The impact of patient-specific inlet conditions on oscillatory shear and helicity in haemodynamic simulations of aneurysmal Type-B Aortic Dissection

C. Stokes[1,2], D. Ahmed[3], N. Lind[4], F. Haupt[4], D. Becker[5], J. Hamilton[1]
V. Muthurangu[6], H. von Tengg-Kobligk[4], G. Papadakis[3]
S. Balabani[1,2], V. Diaz-Zuccarini[1,2]

Affiliations: [1]Department of Mechanical Engineering, University College London, London, UK [2]Wellcome-EPSRC Centre for Interventional Surgical Sciences, London, UK [3]Department of Aeronautics, Imperial College London, London, UK [4]Department of Diagnostic, Interventional and Pediatric Radiology, Inselspital, University of Bern, Switzerland [5]Centre for Translational Cardiovascular Imaging, University College London, United Kingdom [6] Clinic of Vascular Surgery, Inselspital, University of Bern, Switzerland

Correspondence: V. Diaz-Zuccarini, Department of Mechanical Engineering, University College London, London, UK e-mail: `v.diaz@ucl.ac.uk`

Abstract

Type-B Aortic Dissection (TBAD) is cardiovascular disease in which a tear develops in the intimal layer of the descending aorta, allowing pressurised blood to delaminate the intimal and medial layers to form a true and false lumen. In medically managed patients, long-term aneurysmal dilatation of the false lumen is considered virtually inevitable and is associated with poorer disease outcomes. The pathophysiological mechanisms driving false lumen dilatation are not yet understood, though haemodynamic factors are believed to play a key role. Recent analysis via Computational Fluid Dynamics (CFD) and 4D-Flow MRI have demonstrated links between flow helicity, oscillatory wall shear stress and aneurysmal dilatation of the false lumen. In this study, we compare simulations using the gold-standard three-dimensional, three-component inlet velocity profile (3D IVP) extracted from 4DMR data with flow-matched flat and through-plane profiles that remain widely used in the absence of 4DMR. Furthermore, we assess the impact of 4DMR imaging errors on the flow solution by scaling the 3D IVP components to the degree of imaging error observed in previous studies. We demonstrate that secondary inlet flows affect the distribution of oscillatory shear and helicity throughout the FL, and that even the 3D IVP exhibited notable differences in helicity and oscillatory shear when modulated to account for imaging errors. These results illustrate that the quality of inlet velocity conditions in simulations of TBAD may greatly affect their clinical value, and efforts to further enhance their patient-specific accuracy are warranted.

keywords: Computational Fluid Dynamics, Aortic Haemodynamics, Aortic Dissection, patient-specific, 4D-Flow MRI, Inlet Conditions, Inlet Velocity Profile

1 Introduction

Type-B Aortic Dissection (TBAD) is treated medically in the absence of complications. Despite the use of anti-hypertensive treatment, aneurysmal growth of the aorta is observed in up to 87% of these medically treated patients[36], usually with more pronounced growth in the thoracic aorta[5,38]. Aortic growth is a known risk factor for late adverse events including aortic rupture, so there is value from a clinical perspective in understanding how and why this growth occurs; predictors of aneurysmal growth may be used to tailor treatment and improve disease outcomes[36,16]. Unfortunately, these pathological mechanisms are not yet well-understood and existing anatomical predictors of aortic growth, including a large false lumen (FL) diameter at presentation and a large, proximally located primary entry tear (PET)[40], perform poorly[26,10]. Better risk stratification tools are needed.

Haemodynamic quantities such as pressure and Wall Shear Stress (WSS) may offer greater predictive value than anatomical markers as they are more directly linked with the physiological mechanisms at play; WSS characteristics are known to influence the behaviour of endothelial cells while fluid pressure exhibits structural forces on arterial tissue. Greater FL flow[35,33] and pressurisation[50,44,51] have been associated with aortic growth, in addition to retrograde flow through the PET[26,7]. The latter has been associated with increased FL pressurisation. Regions of high oscillatory shear index (OSI) and low time-averaged WSS (TAWSS) have been linked with aneurysmal growth and rupture[12,41] in TBAD and other aortic diseases[12,33,18,21], creating a feedback loop of degradation as growth further exacerbates these effects[41].

Despite the growing evidence of haemodynamic involvement in TBAD progression, links remain unclear and further research is needed to develop robust, clinically applicable haemodynamic predictors. 4D-Flow MRI (4DMR) and Computational Fluid Dynamics (CFD) are the two predominant means of haemodynamic analysis, but efforts to understand and limit the errors and uncertainties associated with these modalities are still needed. 4DMR is known to perform poorly in regions with low velocity[23] and its resolution is not sufficient to capture high velocity gradients, both leading to large uncertainties in extracted WSS indices[49] and limiting its use in understanding flow-mediated aneurysmal growth. CFD offers high spatiotemporal resolution but patient-specific accuracy is strongly influenced by segmentation quality, the choice of boundary conditions and various other modelling assumptions. Applying patient-specific boundary conditions in CFD from 4DMR data is currently the most favourable means of producing accurate, high-fidelity haemodynamic data. As 4DMR data is not routinely acquired, simplified or literature-based boundary conditions are frequently used, despite the knowledge that this can have a profound impact on the accuracy of the results.

While the impact of inlet conditions on velocity magnitude and TAWSS have been investigated in TBAD[1,24], these efforts did not consider oscillatory shear indices or flow helicity, each of which are associated with aneurysmal growth in TBAD[33,34] and have shown substantial sensitivity to inlet conditions in healthy aortae[28]. In this study, we explore the impact of several widely used inlet conditions on disturbed shear indices and flow helicity in a case of chronic TBAD. In this patient, widespread aneurysmal growth of up to 88% was observed in the FL over two years. We compare the gold-standard three-dimensional, three-component inlet velocity profile (3D IVP) extracted from 4DMR data with flow-matched flat (F) and through-plane (TP) profiles that remain widely used in the absence of 4DMR. Furthermore, we assess the impact of 4DMR imaging errors on the flow solution by scaling the 3D IVP components down to the degree of velocity underestimation observed in previous studies[11].

To further examine the impact of inlet conditions on the velocity field, we employ Proper Orthogonal Decomposition (POD), a reduced order modelling (ROM) technique that is becoming more widely used to analyse cardiovascular flows[29,47]. POD is typically used to identify coherent flow structures which optimally capture the fluctuating energy of the velocity field, facilitating a deeper understanding of complex flow fields[2]. POD has been applied to characterise turbulence in cerebral arteries[15,19], examine the impact of inflow strength and angle in cerebral and abdominal aortic aneurysms and identify differences between healthy and pathological flow conditions within them[29,8]. It has also been used to enhance the resolution of 4DMR data in coronary and cerebral arteries[3,27].

2 Methodology

2.1 Clinical data

Medical imaging data from a 56-year-old male patient with chronic TBAD were acquired at [REDACTED] under ethical approval from the local institutional review board (ID: 2019-00556). A Siemens SOMATOM Definition Flash (Siemens AG, Munich, Germany) was used to acquire Computed Tomography Angiography (CTA) data using an isotropic spatial resolution of 0.5mm. Four months after CTA, 4D-Flow MRI (4DMR) data were acquired using a Siemens Aera 1.5T, and again at two years after CTA, using a spatial resolution of 2.25 x 2.25 x 3.00 mm, a velocity encoding (VENC) of 150 cm/s and 16 timeframes across the cardiac cycle. A heart rate of 94 beats per minute was extracted from the 4DMR data and a single brachial measurement of 138/81 was obtained before the first 4DMR acquisition. Luminal area measurements were extracted from each 4DMR dataset at 5mm increments along the thoracic aorta, indicating that over the two years between acquisitions, the thoracic FL dilated by an average of 35% and a maximum of 88%.

2.2 Segmentation & Meshing

The computational domain, extending from the ascending aorta to the distal end of the dissection at the external and internal iliac arteries, was manually segmented from CTA data using Simpleware ScanIP (Synopsys Inc., CA, USA) and Autodesk Meshmixer (Autodesk Inc., CA, USA) and non-rigidly registered to the 4DMR domain using a continuous-point-drift algorithm in MATLAB (Matlab, Natick, MA, USA). For later analysis, the volume was divided into five sections: the ascending aorta (AA), the thoracic TL and FL (TL_t and FL_t), and the abdominal TL and FL (TL_a and FL_a) as shown in Fig. 1.

The volume was meshed using tetrahedral elements in Fluent Mesh (ANSYS Inc., PA, USA). Mesh sizing parameters were determined with a mesh independence study described in Supplementary Material SM1. The final mesh contained 2.30M elements, including ten near-wall layers and a first-cell-height corresponding to a mean y+ of 0.83 at peak systole.

The primary entry tear (PET), located at the left subclavian artery (LSA), is ≈18mm in diameter. The first and largest re-entry tear is located 170mm distal to the PET, as indicated in Fig. 1. Nineteen further luminal communications are present, many near the abdominal branches.

2.3 Inlet conditions

We will compare simulations with four commonly used patient-specific inlet velocity profiles (IVP), each derived from the first: a three-component, three-dimensional (3D) IVP which precisely matches the magnitude and direction of 4DMR velocities at the inlet plane, as shown in Fig. 1. A flat (F) IVP was generated with an identical inlet flow waveform (Q_{in}), but with a uniform velocity distribution in the plane-normal direction, as is typically deployed when flow MRI data is not available. Next, a through-plane (TP) IVP was produced, comprising only the plane-normal component of the 3D IVP such that Q_{in} was matched. Through-plane IVPs may be used when only 2D Flow MRI data is available. The final profile was identical to the 3D IVP, but with each velocity component increased by 25%; 4DMR data has been shown to underestimate peak flow rate and velocity by ≈20-30%[11] depending

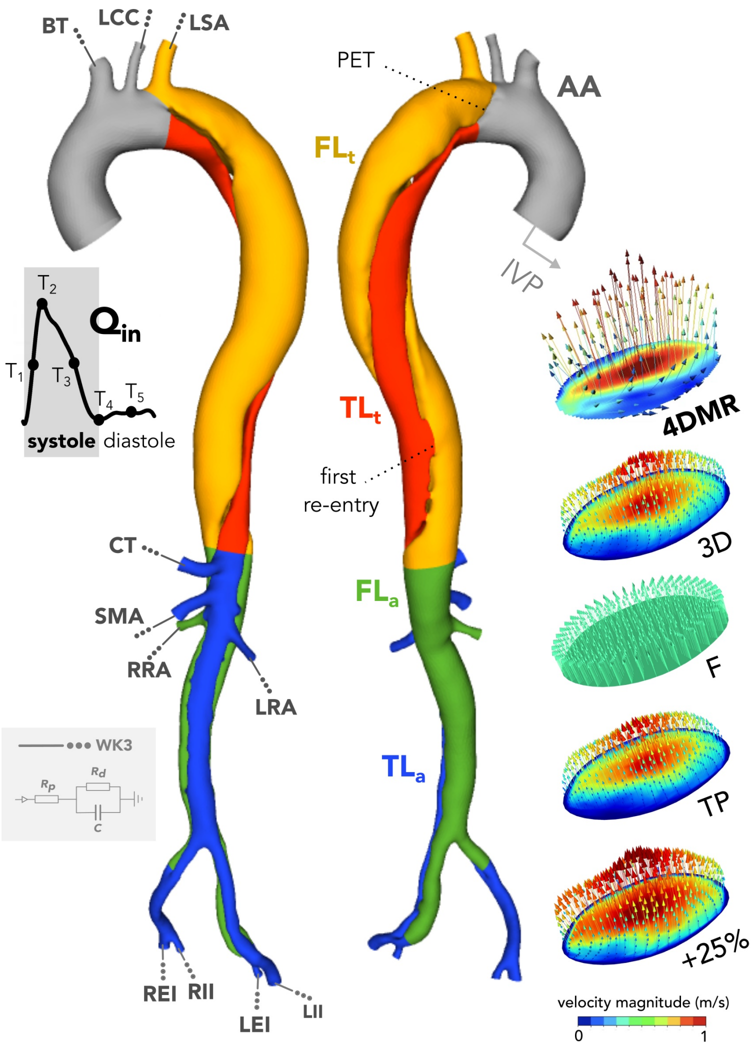

Figure 1: *The computational domain with schematic depictions of inlet and outlet boundary conditions. The velocity magnitude contours and vectors at peak systole of each patient-specific inlet velocity profile are provided bottom right. The coloured regions of the aortic geometry represent the analysis regions used for helicity computations.*

on image resolution. The stroke volume of this IVP is thus 25% higher than the other three IVPs.

To produce the 3D IVP, from which all other conditions were produced, velocity data from 4DMR was first extracted at the inlet plane using GTFlow (Gyrotools LLC, Zurich, CH). Individual contours were generated at each imaging time point to track the ascending aortic wall as it translated and expanded across the cardiac cycle. As the CFD inlet shape and location is fixed in time, and simulations require a higher temporal and spatial resolution than 4DMR provides, an algorithm was developed to register and interpolate the 4DMR data onto the CFD inlet to generate the 3D IVP. First, the 4DMR contour region from each timeframe was mapped to the CFD inlet using non-rigid continuous point drift in MATLAB. By definition, non-rigid registration does not preserve the distance between spatial points and may excessively distort the velocity profile. However, rigidity parameters were kept high and 4DMR contours regions closely matched the circular shape of the CFD inlet, thus preventing excessive distortion. The registered component velocity field at each timestep was then spatially interpolated onto a fixed, uniform grid to facilitate temporal interpolation to match the simulation timestep. Temporal spline interpolation was performed over numerous cardiac cycles to ensure a smooth flow waveform. Points at the perimeter of the inlet were set to zero velocity to align with the non-slip wall boundary condition. Finally, spatial interpolation of the IVP onto the inlet mesh was performed automatically by the solver, ANSYS CFX 2020.

2.4 Outlet boundary conditions

Patient-specific flow and pressure distributions were reproduced in each simulation using three-element Windkessel (WK3) outlet boundary conditions. Target systolic and diastolic pressures (P_s and P_d) were derived as follows:

$$P_d \approx P_d' \tag{1}$$

$$P_s \approx 0.83P_s' + 0.15P_d' \tag{2}$$

where P_s' and P_d', are the patient's brachial systolic and diastolic pressure measurements[42]. The same pressure targets were used for all simulations.

Mean outlet flow rates were extracted from 4DMR at each major branch using GTFlow. Due to image resolution, measurement uncertainties in 4DMR are higher in these smaller branches than the aorta. To mitigate the effects of this uncertainty, the mean flow rate

	$\overline{Q}$ ml/s						R^{tot}_{WK3} mmHg/ml/s		C_{WK3} ml/mmHg	
	Target	**3D**	**F**	**TP**	+25%	ρ	3D	+25%	3D	+25%
BT	17.10	17.69	17.00	17.47	22.11	0.030	5.77	4.37	0.24	0.63
LCC	3.84	3.97	3.77	3.89	4.88	0.030	25.67	19.43	0.05	0.14
LSA	6.69	6.98	6.63	6.83	8.57	0.030	14.75	11.16	0.09	0.25
CT	16.31	16.14	15.56	16.06	19.95	0.056	6.05	4.58	0.22	0.59
SMA	14.09	13.86	13.41	13.85	17.24	0.056	7.00	5.30	0.19	0.51
LR	16.59	15.63	15.49	15.72	19.00	0.280	5.94	4.50	0.23	0.61
RR	12.64	12.25	12.02	12.19	14.88	0.280	7.80	5.90	0.17	0.46
LEI	9.61	9.60	9.26	9.56	11.85	0.056	10.26	7.76	0.13	0.35
LII	4.76	4.76	4.58	4.72	5.90	0.056	20.72	15.68	0.07	0.17
REI	5.21	5.41	5.15	5.29	6.69	0.056	18.95	14.34	0.07	0.19
RII	3.01	3.17	3.00	3.07	3.98	0.056	32.79	24.81	0.04	0.11

Table 1: *Outlet mean flow rates and WK3 parameters in each simulation and at each outlet shown schematically in Fig. 1.* ρ *indicates the proportion of* R_{tot} *attributed to* R_1 *in each WK3. WK3 parameters were identical between 3D, F and TP, but altered in +25% to account for the additional inlet flow volume.*

at each outlet was scaled proportionally by the mean flow difference between aortic planes upstream and downstream of its containing group of branches (supra-aortic, abdominal, iliac). For the +25% case, target $\overline{Q}$ was increased by 25% at every outlet.

Using these pressure and flow targets, along with the inlet waveform extracted from the 3D IVP, WK3 parameters were tuned using a 0D lumped parameter model of the aorta in 20-sim using our previously-developed techniques[37,6]. The final WK3 parameters are shown in Table 1 alongside the target and simulated mean outlet flow rates for each IVP ($\overline{Q}$). WK3 parameters were identical in the 3D, F and TP cases, but adjusted to maintain the target pressure range in the +25% case.

2.5 Simulation

Transient simulations were performed using ANSYS CFX 2020 R2 using timesteps of 1ms until cyclic periodicity was reached, characterised by $< 1\%$ change in systolic and diastolic pressures between subsequent cycles. The Reynolds-Averaged Navier-Stokes and contiunity equations were solved numerically using the implicit, second-order backward-Euler method and a root-mean-square residual target of 10^{-5} for all equations within each timestep. Walls were modelled as rigid with a no-slip condition as Cine-MRI data was not available to tune patient-specific aortic compliance using our previously developed techniques[6,37].

Blood was modelled as an incompressible, non-Newtonian fluid using the Tomaiuolo formulation[39] of the Carreau-Yasuda viscosity model and a fluid density of 1056 kg/m^3. The estimated[31,9] peak Reynolds number of 11646 greatly exceeded the critical[31] Reynolds number of 6959, thus the k-ω Shear Stress Transport (SST) Reynolds-averaged turbulence model was deployed using a low turbulence intensity (1%) at non-wall boundaries[22].

2.6 Flow Analysis

This section will describe the various techniques applied to analyse the results of the simulations and differences between them.

2.6.1 Wall Shear Stress

Using every fifth timestep from the final cardiac cycle, the Time Averaged Wall Shear Stress (TAWSS), Oscillatory Shear Index (OSI), Relative Residence Time (RRT), and Endothelial Cell Activation Potential (ECAP) were computed as follows:

$$TAWSS = \frac{1}{T}\int_t^{t+T} |\boldsymbol{\tau}| dt \tag{3}$$

$$OSI = \frac{1}{2}\left(1 - \frac{\left|\frac{1}{T}\int_t^{t+T} \boldsymbol{\tau} dt\right|}{\frac{1}{T}\int_t^{t+T} |\boldsymbol{\tau}| dt}\right) \tag{4}$$

$$RRT = \frac{1 - 2 * OSI}{TAWSS} \tag{5}$$

$$ECAP = \frac{OSI}{TAWSS} \tag{6}$$

$$\tag{7}$$

where $\boldsymbol{\tau}$ is the instantaneous WSS vector[20].

2.6.2 Helicity

We will assess the impact of IVP on bulk flow structure via qualitative and quantitative comparison of helicity. Helicity, $H(t)$, is a scalar property used to identify streamwise vortical structures by quantifying the local alignment of velocity and vorticity vectors, $\mathbf{v}(\mathbf{x}, t)$ and $\boldsymbol{\omega}(\mathbf{x}, t)$, over a volume V:

$$H(t) = \int_V \mathbf{v}(\mathbf{x}, t) \cdot \boldsymbol{\omega}(\mathbf{x}, t) dV = \int_V H_k(\mathbf{x}, t) dV \tag{8}$$

where H_k is the helicity density[13]. $H(t)$ can also be evaluated over a single 2D plane by integrating the same quantities over its area. The sign of H_k indicates the direction of rotation relative to the velocity vector: positive values indicate right-handed helices (clockwise), while negative values are left-handed (anti-clockwise). As $H(t) = 0$ can indicate either the presence of symmetrical counter-rotating vortices, or zero velocity/vorticity, the magnitude of helicity can be used to distinguish these scenarios:

$$|H(t)| = \int_V |H_k|(\mathbf{x}, t)dV \tag{9}$$

Helical flow is a natural feature of healthy aortic flow[10] and has been demonstrated to suppress flow disturbances in cerebral aneurysms[13]. As helical structures in the aorta are on a larger scale than the fluid boundary layer, these flow features can be measured more reliably with 4DMR than WSS measurements. As a result, associations between helicity and WSS are sought due to the potential predictive power and clinical value of WSS[13,10].

Local Normalised Helicity (LNH), defined as:

$$LNH(\mathbf{x}, t) = \frac{H_k(\mathbf{x}, t)}{|\mathbf{v}(\mathbf{x}, t)||\boldsymbol{\omega}(\mathbf{x}, t)|} \tag{10}$$

is often used to visualise vortical structures in the aorta by plotting isosurfaces of LNH at equal but opposing-sign values, in this case, ±0.6. Quantitative assessment of helicity can be performed by averaging H_k over a defined volumetric region, V, and time interval, T:

$$h_1 = \frac{1}{TV}\int_T \int_V H_k dV dt \tag{11}$$

$$h_2 = \frac{1}{TV}\int_T \int_V |H_k| dV dt \tag{12}$$

$$h_3 = \frac{h_1}{h_2} \tag{13}$$

where h_1 is 0 either with reflectional symmetry in helical structures or with no velocity or vorticity. h_2 quantifies the total amount of helicity in the volume regardless of direction. h_3 is a value between -1 and 1 whose magnitude reflects the relative balance between right- and left-handed helicity, and its direction. Helicity indices h_1-h_3 were computed across the full cardiac cycle, and across systole and diastole in the five aortic subdomains depicted in Fig. 1: AA, TL_t, FL_t, TL_a and FL_a.

2.6.3 Proper Orthogonal Decomposition

POD decomposes a chosen flow property into a set of spatial modes, each of which are modulated by a time coefficient. In this study, we consider the flow velocity $\mathbf{v}(x, y, z, t)$ with the independent variables x, y, z in space and in time, t. $\mathbf{v}^{'}(x, y, z, t)$ represents the fluctuating velocity about the mean, i.e. $\mathbf{v}^{'}(x, y, z, t) = \mathbf{v}(x, y, z, t) - \overline{\mathbf{v}}$, where $\overline{\mathbf{v}}$ is the temporal mean of $\mathbf{v}(x, y, z, t)$. Applying POD, $\mathbf{v}^{'}(x, y, z, t)$ is decomposed into spatial modes, $\Phi(x, y, z)$, each associated with a time coefficient $a(t)$, as follows:

$$\mathbf{v}^{'}(x, y, z, t) = \sum_{k=1}^{\infty} a_k(t)\ \Phi_k(x, y, z) \tag{14}$$

where k is the number of the mode. Modes are ordered by energy content. The ‘zeroth’ POD mode represents the time-averaged flow $\mathbf{v}$, while all higher modes represent time-dependent flow structures[19]. The spatiotemporal resolution of 4DMR data is insufficient for POD analysis, so higher-fidelity 2D or 3D velocity data from Particle Image Velocimetry (PIV) and CFD are typically used in this process[19]. In this work, POD analysis was performed in MATLAB using velocity snapshots throughout the full aorta at 5ms increments across the final cycle of each CFD simulation.

The energy-based ranking of modes is performed such that the flow can be accurately reconstructed using a discrete quantity of these modes[2], thus reducing the order of the system. The flow is said to be accurately represented by the ensemble of modes containing 98% of the total KE which, in cardiovascular flows, has been widely reported to occur within the first 1-10 modes[17,29,8,48].

Due to the energy-based nature of this analysis, modes may not retain physical interpretability due to frequency mixing[2]. Nevertheless, POD analysis offers a means of examining how the fluid KE is distributed amongst coherent flow structures and how this energy changes over time, facilitating a decoupling of spatial and temporal behaviour which can provide valuable insights into the behaviour of the flow[29]. For example, POD analysis of the flow in ruptured and unruptured aneurysms showed that rupture was more strongly associated with spatial flow complexity, rather than temporal stability[8]; similar insights may be available in the context of aneurysmal TBAD.

3 Results

In this section, we will compare velocity, pressure, helicity and WSS distributions across the cardiac cycle both qualitatively and quantitatively. We refer to time instants T_1 to T_5 across the cardiac cycle, as depicted schematically in Fig. 1. Emphasis will be placed on the thoracic aorta as this is where growth of the aorta is mainly observed, and because 4DMR measurements from the abdominal aorta and iliac arteries are not fully reliable due to the low spatial resolution of images in that region. Furthermore, we provide POD analysis of the velocity field to assess how each inlet condition affects the coherent structures within the flow and the distribution of energy amongst them.

3.1 Velocity

Velocity magnitude contours at mid-deceleration (T_3) from 4DMR and each simulation are shown in Fig. 2 and for other time instants in Supplementary Material SM2. Velocity distribution in the 3D case agrees closely with 4DMR throughout the cardiac cycle. However, velocity magnitude is lower in 4DMR than CFD in both lumens. 4DMR is known to perform poorly in low-velocity regions such as the FL, and to underestimate peak velocity[23,11]. Additionally, the cycle-averaging inherent in 4DMR data may affect velocity magnitude measurements in regions experiencing highly unsteady flow (e.g. beyond the PET), and the low spatial resolution of 4DMR cannot resolve small-scale flow features. Imaging uncertainties are likely to account for many of the differences observed between 4DMR and CFD. As such, the 3D IVP case will be considered the gold-standard, with each IVP case compared against it. This approach has been taken in other studies[1].

Between IVP cases, TL velocity distributions are qualitatively similar but with higher velocity magnitudes in the +25% case. Qualitative differences between cases are primarily observed in the ascending aorta (planes a and b) and mid-thoracic FL (planes d-g). To quantify and further assess these differences, we compared the Pearson correlation coefficients of velocity magnitude on each analysis plane between each IVP and the 3D IVP at five points across the cardiac cycle. These results are shown in Fig. 3 , while details on our calculation methods can be found in Supplementary Material SM3.

During flow acceleration (T_1), velocities are well correlated with exception to the proximal FL in all cases at plane f, and on plane c in the +25% case. At peak systole (T_2), velocities are highly correlated throughout, with marginal decorrelation on planes c and f. During flow deceleration (T_3), poorest correlation is observed in the ascending aorta, with

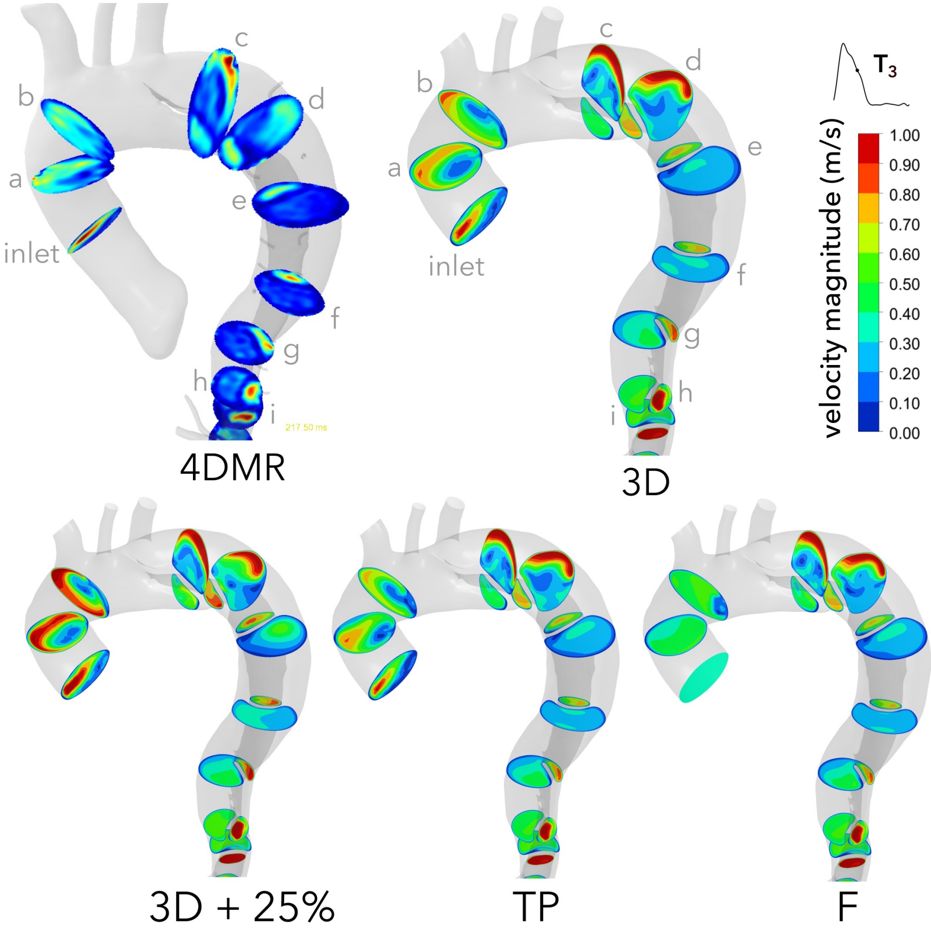

Figure 2: *Contours of velocity magnitude in the thoracic aorta at mid-deceleration (T_3) in each case, compared with 4DMR. Note that velocity contours are clipped to 1 m/s for clarity, but velocity reaches up to 1.3 m/s. Similar contours are provided at T_2 and T_4 in Supplementary Material SM2*

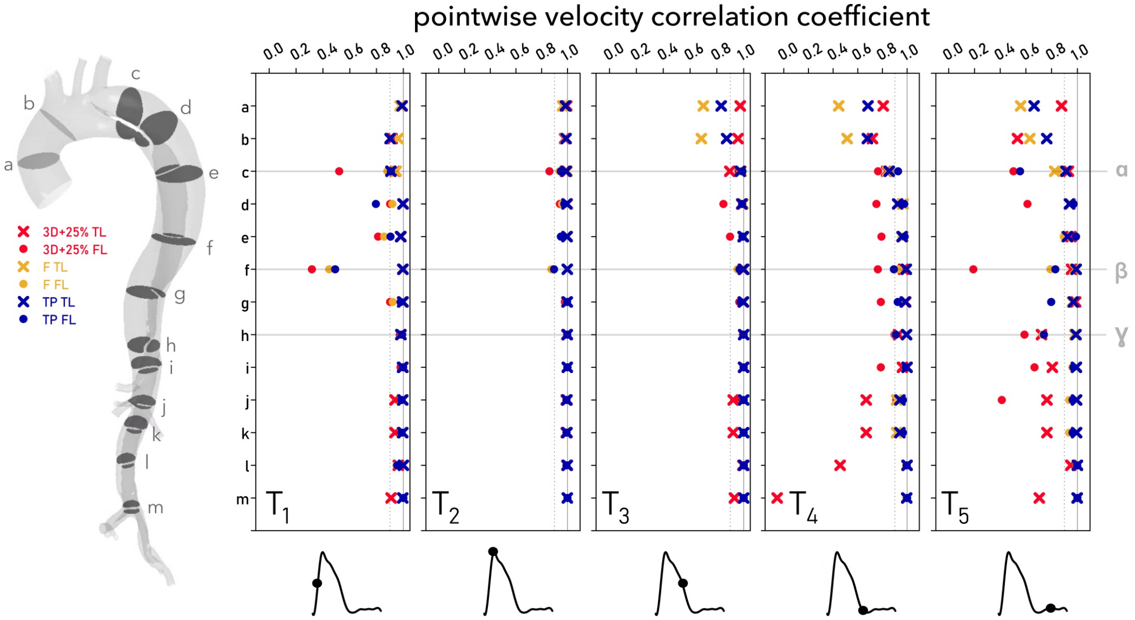

Figure 3: *Pearson correlation coefficients between 3D IVP velocity magnitude and each other case at T_1 to T_5. Coefficients were computed by comparing every node on each indicated plane along the length of the dissection following the method described in Supplementary Material SM3. TL and FL points are distinguished by using different symbols.*

case F decorrelating most, followed by TP and +25%. During diastole, at T_4 and T_5, poor correlation prevails in the ascending aorta in all cases. The +25% case decorrelates particularly strongly in the FL and the abdominal TL, even reaching negative correlation at T_4. Throughout the cycle, planes c and f exhibit poor agreement in each case. These planes align closely with the most aneurysmal regions of the FL, as will be discussed further below.

3.2 Pressure

Simulated systolic, diastolic and pulse pressures are shown alongside target values in Table 2. The simulated False Lumen Ejection Fraction (FLEF), calculated as the retrograde flow through the PET as a proportion of the total stroke volume, is shown alongside the target value extracted from 4DMR data. FLEF has been identified as a flow-based proxy for FL pressurisation and has been associated with increased aortic growth rate in TBAD[14]. The range of mean transmural pressure (TMP) is also indicated for each simulation: $TMP = P_{TL} - P_{FL}$, where TL and FL pressures are evaluated as the mean static pressure across a cross-sectional plane through the aorta. TMP magnitudes greater than 5 mmHgare associated with aortic growth in TBAD[49]. Changes in TMP along the dissection

	3D	**Flat**	**TP**	**+ 25%**	**Measurement**
P_s (mmHg)	127.8	129.6	128.8	133.2	$127^{\dagger}$
P_d (mmHg)	80.4	80.8	80.9	83.5	81
P_{pulse}	47.4	48.8	47.8	49.7	46
FLEF (%)	0.14	0.00	0.00	0.00	2.13
Min. TMP (mmHg)	-1.93	-1.97	-1.96	-2.48	
Max. TMP (mmHg)	1.56	1.39	1.44	1.84	

Table 2: *Pressure metrics from each case alongside the target measured values. † indicates that the systolic pressure measurement is derived from the brachial pressure rather than measured directly.*

will be discussed later in this section.

Despite substantial aortic growth in this patient, measured FLEF is only 2.1% and mean TMP reaches only 2 mmHg, likely due to the presence of numerous large intra-luminal communications throughout the dissection which minimise pressure and flow gradients between them. Only the 3D IVP predicts any degree of retrograde flow. The rigid-wall assumption is likely to affect this metric as aortic compliance acts as a pump; FL compliance *in vivo* will store elastic energy during systole and may impart this energy as momentum back through the PET during diastole.

Even with identical inlet flow rate waveforms and outlet boundary conditions, the flat IVP exhibits a 3% higher pulse pressure than the 3D IVP while the TP case exceeds the 3D case by less than 1%. Maximal TMP (greater TL pressurisation) reaches lower magnitudes than 3D in cases F and TP while minimum TMP (greater FL pressurisation) reaches higher magnitudes. This indicates that the FL is relatively more pressurised in F and TP than in 3D. TMP reaches greater magnitudes in +25%; Minimum TMP is 28% lower than the 3D case while maximum TMP is only 18% higher. This negative shift again indicates more relative pressurisation of the FL.

3.3 Helicity

LNH isosurfaces during mid-deceleration (T_3) are shown in the TL and FL in Fig. 4 alongside plots of $H(t)$ and $|H(t)|$ across the cardiac cycle. Bulk helicity indices h_1 - h_3 in each sub-domain are provided in Table 3.

Helical strength, shown as a distribution of $|H(t)|$ in Fig. 4 and characterised by the magnitude of h_2 in Table 3, is greatest during the decelerating portion of the cardiac cycle[10]. Helical strength in cases 3D, F and TP match closely everywhere except the AA, where

$\%_{3D}$		systole			diastole			full cycle		
		h_1	h_2	h_3	h_1	h_2	h_3	h_1	h_2	h_3
AA	3D	1.61	23.54	0.07	-2.06	3.67	-0.56	-0.22	13.44	-0.02
	F	-2.21	11.58	-0.19	-0.72	1.11	-0.65	-1.43	6.25	-0.23
	TP	-2.00	19.05	-0.11	-0.72	2.45	-0.29	-1.35	10.61	-0.13
	+25%	3.21	38.15	0.08	-0.93	4.70	-0.20	1.12	21.29	0.05
$\mathbf{TL_t}$	3D	10.72	26.12	0.41	1.65	3.13	0.53	6.15	14.53	0.42
	F	10.36	24.84	0.42	1.18	2.51	0.47	5.74	13.59	0.42
	TP	10.99	25.36	0.43	1.28	2.52	0.51	6.05	13.75	0.44
	+25%	14.04	34.52	0.41	3.08	5.94	0.52	8.46	19.98	0.42
$\mathbf{FL_t}$	3D	1.58	7.73	0.20	0.01	1.59	0.01	0.79	4.63	0.17
	F	1.26	7.65	0.17	0.29	1.77	0.16	0.77	4.69	0.16
	TP	0.87	7.39	0.12	0.09	1.68	0.05	0.47	4.48	0.11
	+25%	1.56	9.69	0.16	-0.11	2.20	-0.05	0.71	5.85	0.12
$\mathbf{TL_a}$	3D	16.34	98.91	0.17	0.84	6.16	0.14	8.53	52.17	0.16
	F	17.20	99.29	0.17	0.60	5.77	0.10	8.83	52.16	0.17
	TP	16.84	97.88	0.17	0.67	5.74	0.12	8.62	51.06	0.17
	+25%	19.99	120.17	0.17	3.92	12.72	0.31	11.89	66.02	0.18
$\mathbf{FL_a}$	3D	1.18	13.22	0.09	-0.51	2.06	-0.25	0.33	7.60	0.04
	F	1.73	13.64	0.13	-0.44	2.01	-0.22	0.63	7.78	0.08
	TP	1.49	13.41	0.11	-0.49	1.97	-0.25	0.49	7.59	0.06
	+25%	2.34	17.01	0.14	-0.06	3.46	-0.02	1.11	10.06	0.11

Table 3: *Bulk helicity indicators* h_1*-*h_3 *for each IVP case. Indices are computed across systole, diastole, and the full cycle within each aortic subdomain as indicated in Fig. 1.*

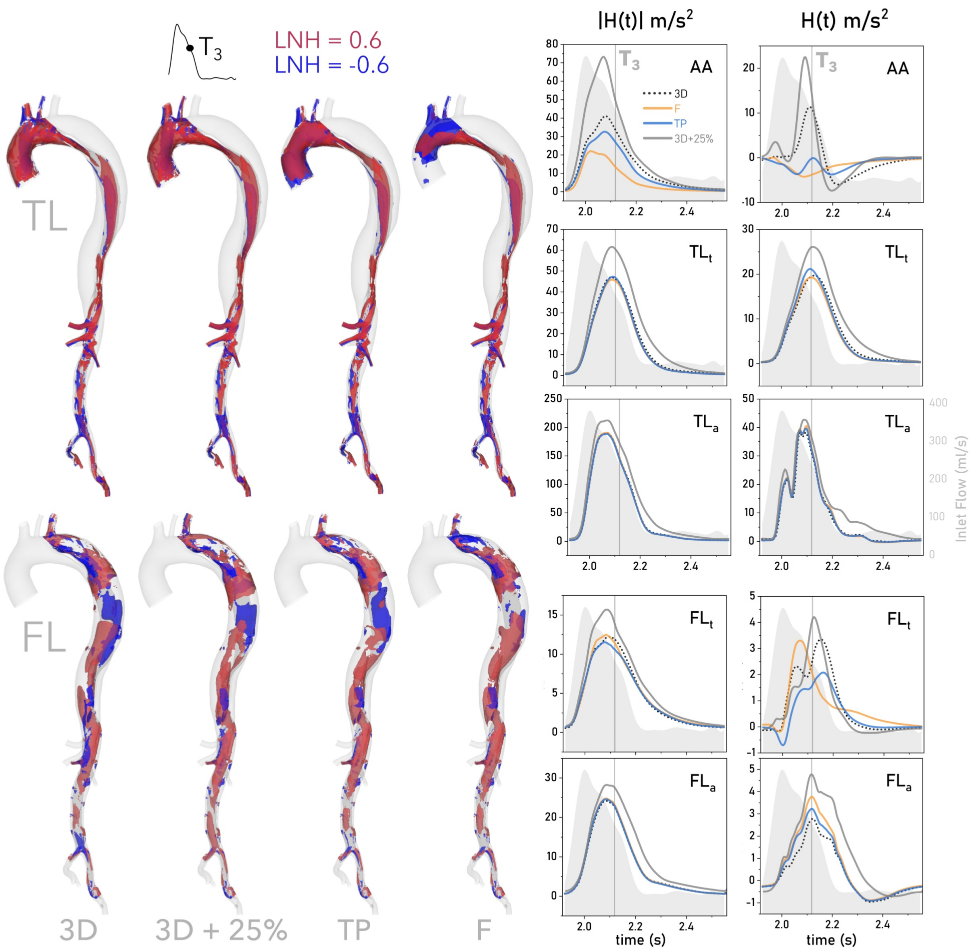

Figure 4: *Isosurfaces of LNH* $= \pm 0.8$ *from each IVP case at mid-deceleration* (T_3) *within the TL and FL individually (left). LNH contours at additional time points, and the time-averaged LNH, are provided in Supplementary Material SM4. Time evolution of* $H(t)$ *and* $|H(t)|$ *within each subdomain shown in Fig. 1 are provided on the right, with* T_3 *indicated as a vertical reference line. The inlet flow rate is shown as a grey shaded region in each helicity plot using a secondary y-axis, scaled identically across all plots.*

helicity is weaker when in-plane velocity components are neglected, as observed in other studies[28,32]. The +25% case provides greater helical strength throughout the domain and particularly in the AA.

Healthy aortae typically exhibit positive helicity in the AA and negative helicity beyond the mid-thoracic descending aorta[10]. Removing in-plane inlet velocity components results in predominantly *negative* helicity in the AA during systole, evidenced by larger blue LNH volumes in Fig. 4 and negative values of h_1. In contrast with healthy aortae, which usually exhibit negative helicity in the descending aorta, each subdomain in this case exhibit dominantly *positive* helicity (h_1) throughout the cycle, except for FL_a where a uniformly negative dominance develops during diastole; the 3D case presents a unique region of broader negative (blue) LNH near the iliac bifurcation that is not observed in other cases.

While minimal differences in $H(t)$ and h_1 are observed throughout the TL, except for the +25% case, which exhibits greater helicity magnitude, substantial differences are observed throughout the FL in all cases. As shown in Fig. 4, in FL_t, case F exhibits an earlier peak in $H(t)$ than the other cases. As helical strength ($|H(t)|$ and h_2) is very similar between 3D, F and TP cases in this region, this indicates differences in the development of right- and left-handed helical structures during diastole. Indeed, h_3 values indicate a 16-fold increase in clockwise dominance in F compared to 3D. These differences are likely to affect oscillatory shear distributions in the thoracic FL, as will be discussed later.

3.4 Wall Shear Stress

Distributions of TAWSS, OSI, ECAP and RRT in the thoracic aorta are shown for the 3D case in Fig. 5 alongside difference contours with each additional IVP case. The locations of greatest FL growth, sections α and β, are indicated on the 3D ECAP plot. In the thoracic region, TAWSS is highest surrounding and immediately distal to the PET, near section α. TAWSS and differences in TAWSS are minimal throughout the rest of the FL. TAWSS is elevated in the +25% case, particularly in the aortic branches, due to the increased flow volume through them.

In contrast, OSI and ECAP are high throughout the FL, particularly in the mid-thoracic region. OSI and ECAP are noticeably lower in F and +25% cases throughout most of this region, while the TP case shows the greatest similarity with the 3D IVP. Particularly large differences in ECAP are observed between cases at section β. RRT is highest in a concentrated region of the FL where all other cases show considerable differences.

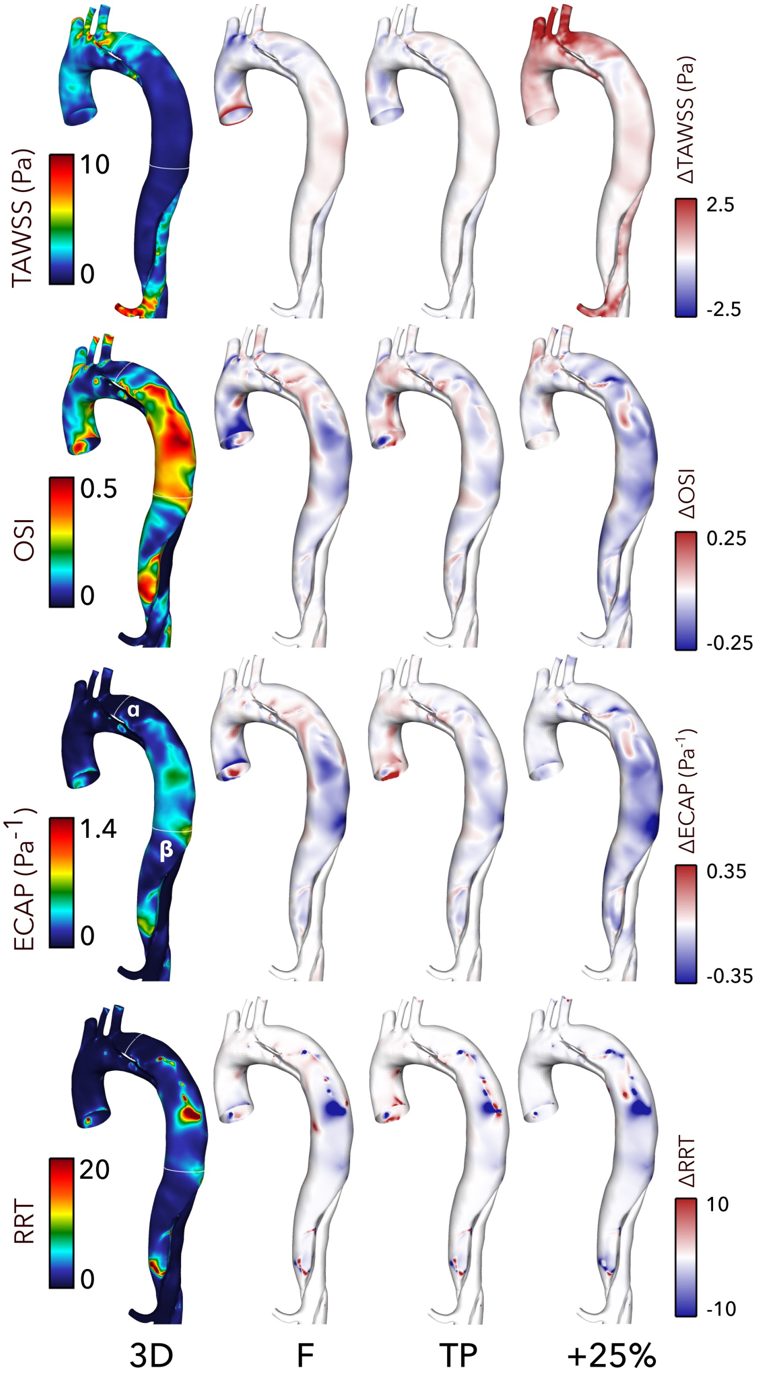

Figure 5: *Contours of TAWSS, OSI, ECAP and RRT in the thoracic aorta from the 3D case (left) and difference contours with each other case (right). Note that contour ranges for TAWSS, ECAP and RRT are clipped for clarity of viewing. Difference contours range from 25-50% of the bounds of the 3D contours.*

3.5 Aneurysmal Growth

We next compare distributions of WSS indices, time-averaged helicity ($\overline{H}$) and helicity magnitude ($|\overline{H}|$), and TMP with measurements of aneurysmal growth along the thoracic FL. Growth is shown as a shaded region in Fig. 6. As mentioned previously, the FL grows most at cross-sections α and β. Marginal FL regression is observed at section γ. On cross-sectional planes co-located with FL area measurements, TAWSS, OSI, RRT and ECAP were circumferentially averaged at the wall and TMP, $H(t)$ and $|H(t)|$ were evaluated as an area-average. These quantities are shown in Fig. 6. The mean discrepancy (Δ_{mean}) and maximum discrepancy (Δ_{max}) of each IVP with the 3D case is indicated as a percentage of the mean 3D value at each point, except $H(t)$. For this variable, the volumetric mean from 3D was used at each point due to the presence of many near-zero values - these values are marked with an asterisk.

TAWSS varies most in the region immediately distal to the PET, up to α, where its magnitude is highest. In this region, oscillatory shear is very low. As TAWSS decreases along the FL, oscillatory shear increases, reaching its maximal values at section β, the location of greatest FL growth. Discrepancies with the 3D case are lowest in TAWSS and greatest in RRT, where a particularly large discrepancy is seen in TP at section β. Maximal and mean errors in each WSS metric are greatest in the +25% case, followed by F, except for ECAP and RRT where greater maximal discrepancies are seen in TP. Oscillatory shear remains elevated at γ where FL regression is observed.

Helicity is strongest up to α, reaching near-zero at β before increasing again beyond γ. The most notable differences between cases occur immediately distal to the PET, but beyond α distributions are similar in all cases. In cases F and TP, $\overline{H}$ varies most in the region immediately distal to the PET with differences also observed in the top half of the FL. $|\overline{H}|$ is nearly identical in distribution in these cases. Conversely, $\overline{H}$ closely matches between 3D and +25% cases, yet $|\overline{H}|$ differs greatly.

TMP distributions are similar in all cases, with greatest magnitudes observed in +25% where TMP is 32% higher on average. TL pressure dominates FL pressure up to the first re-entry tear, where FL pressure begins to dominate. This trend is observed in other computational studies[43]. FL pressurisation is not directly correlated with FL growth in this patient, with growing regions all showing different TMP characteristics; TMP is strongly positive near α, near-zero at β and negative from γ onward.

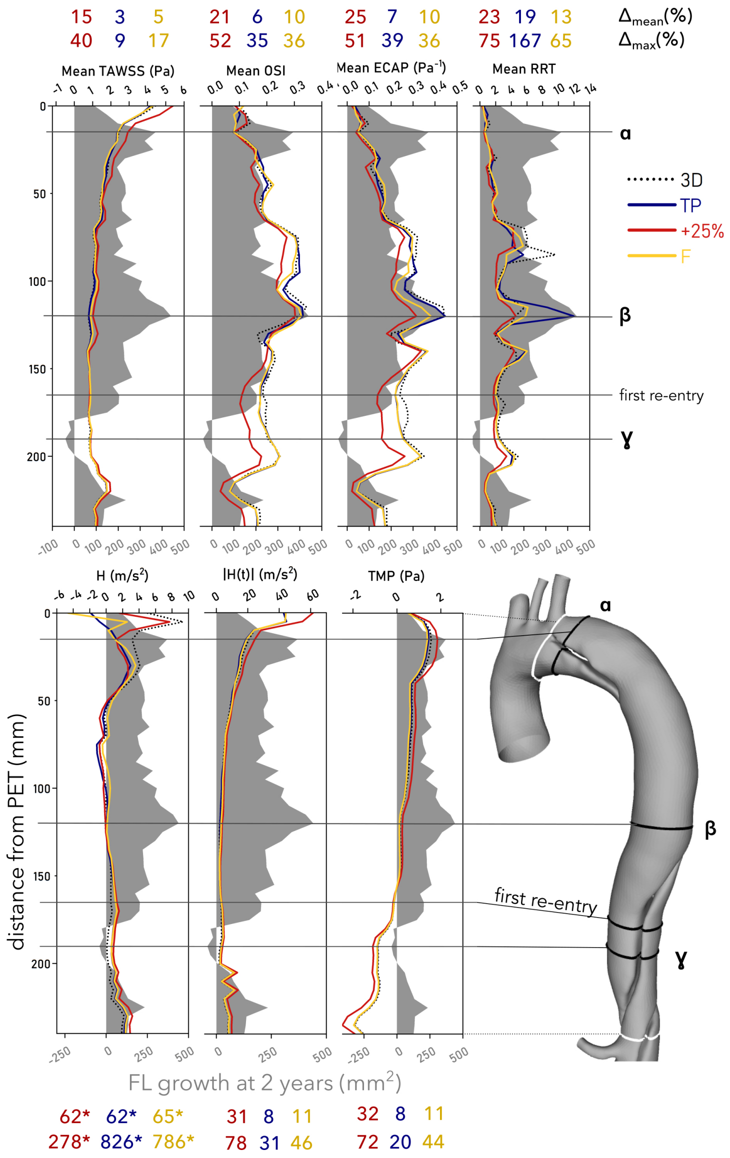

Figure 6: *Circumferentially-averaged TAWSS, OSI, ECAP and RRT (top), plane-averaged H, $|H|$ and TMP (bottom) are plotted along the thoracic FL as a distance from the PET against FL growth (grey shaded area) over a two-year period. Mean and maximum discrepancies (Δ_{mean} and Δ_{max}) between each case and the 3D case are indicated as percentages above/below each plot. The locations of maximum growth are indicated as α and β, the location of FL regression is indicated as γ, and the location of the first re-entry tear is shown.*

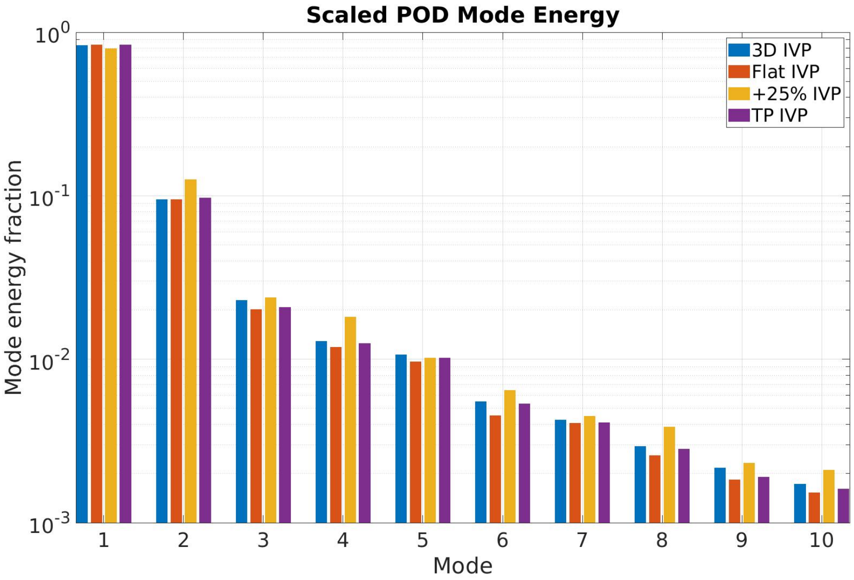

Figure 7: *Histogram of the normalised Kinetic Energy (KE) content of the first 10 modes of the POD. Energy is normalised by the total KE across the first 20 modes within each individual case, which constitute virtually 100% of the total energy.*

3.6 Flow Decomposition

POD was performed using the velocity field from each IVP. Across all IVPs, the first four POD modes capture 96 – 97% of the total normalised KE, which matches observations in other cardiovascular POD analyses[48]. The normalised energy content of mode 1 varies between 79.4% and 84.2% for the different cases, as shown in Fig. 7, with +25% containing the least and F the most.

In the second mode, the +25% case contains the most normalised energy at 12.5% while the other three contain 9.5-9.7%. In the third and fourth modes, the average normalised energy content is only around 2% and 1%, respectively, where the +25% IVP again contains more energy relative to the other cases, a trend which continues to further higher modes. Over 90% of the energy is contained in the first two modes in all cases.

Cross-sectional planes along the ascending and descending aorta were used to investigate the effect of the IVP on each mode, matching those shown in Fig. 2. Fig. 8 compares mode 1 for each of the IVPs. Contours of mode 2 are provided in the Supplementary Material SM5, exhibiting similar trends to those discussed below.

Similarly to the CFD velocity magnitude contours shown in Fig. 2, mode 1 differs greatly in the ascending aorta across all IVPs, as shown in Fig. 8 planes *a* and *b*. While these differences become progressively less apparent along the dissection between 3D, TP

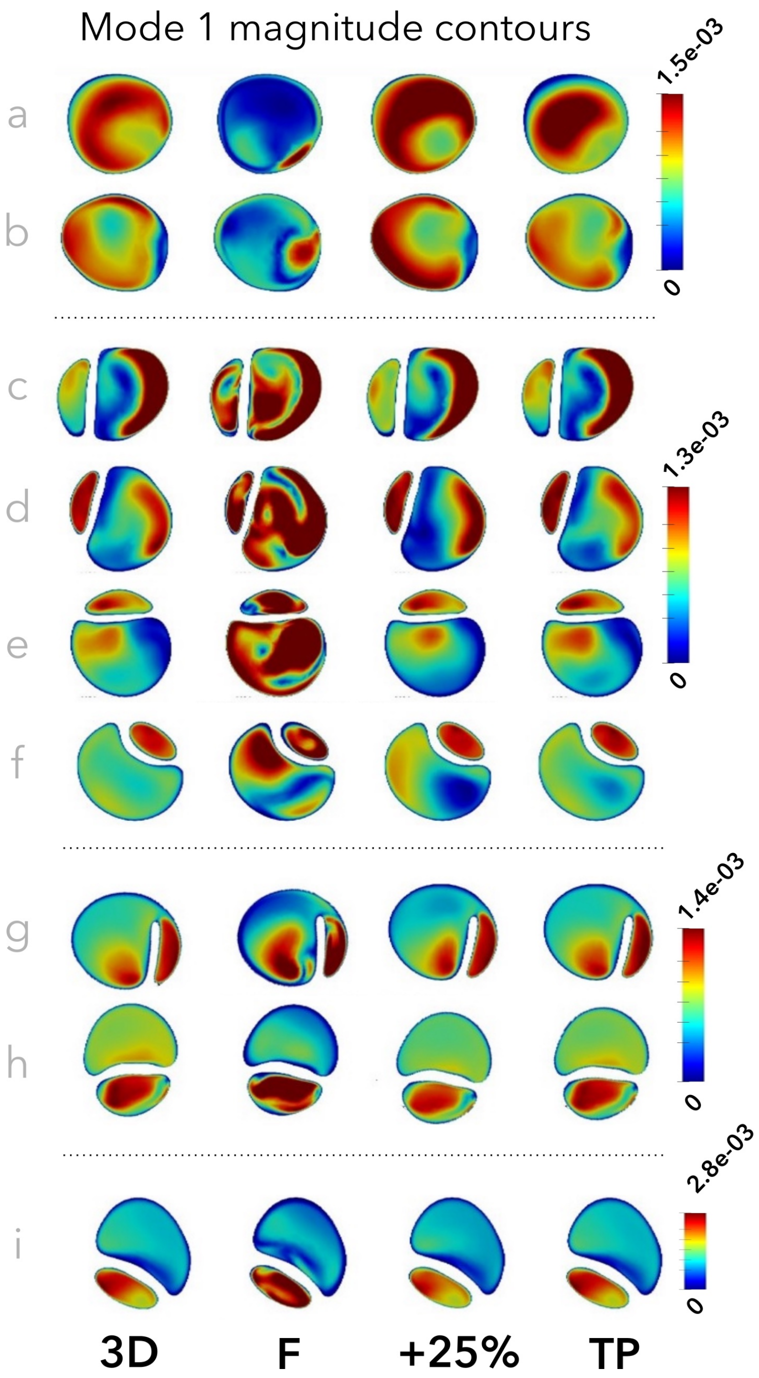

Figure 8: *POD mode 1 at planes (a through i) for the different IVP cases. Note that mode 1 is a 3D vector field; these contours illustrate the magnitude of the local 3D vector. Mode 2 contours are provided in Supplementary Material SM5*

and +25% cases, case F exhibits prominent differences in mode 1 throughout the thoracic aorta (Fig. 8 $c - i$). While 3D and TP IVPs exhibit similarity on most descending aortic planes, some differences are still observed. On plane f , where FL velocity magnitudes were highly decorrelated (Fig. 3), relatively larger differences are observed in the FL between 3D, TP and +25% cases.

4 Discussion

The vast majority of patients with uncomplicated TBAD will experience aneurysmal growth and unfavourable disease progression despite best medical treatment[36]. Haemodynamic predictors extracted from 4DMR-informed CFD may assist clinicians in identifying and optimally treating these patients in future, but a more nuanced understanding of the impact of modelling assumptions, imaging errors and their combined impact on the accuracy of clinically-relevant metrics remains needed. Simulated helicity and osillatory shear have been shown to exhibit greater sensitivity to inlet conditions than other metrics[32,28], but have not been examined in the context of TBAD[1,24] despite links with disease progression[34]. In this work, we have closely examined the sensitivity of oscillatory shear and helicity to inlet conditions in a patient-specific TBAD case, comparing them against FL growth.

Inlet conditions are known to strongly influence velocity, helicity and WSS in the ascending aorta and arch[28,25,46,1,32] and our results firmly corroborate these findings. However, the descending aorta is of greater interest in TBAD, where inlet conditions have been reported to affect qualitative distributions of TAWSS and velocity in the region immediately surrounding the PET whilst minimally affecting distal regions[1,24]. With qualitative assessment alone, our results would provide similar conclusions; velocity magnitude contours and TAWSS distributions appear qualitatively similar throughout the descending aorta. However, the impact of IVP beyond the PET cannot be assessed properly with qualitative analysis; 4DMR cannot adequately resolve this low-velocity and highly aneurysmal region due to low measurement signal, making simulation accuracy of critical importance.

Regions of low TAWSS, which have been directly correlated with aneurysmal growth in AD[45], typically correspond with regions experiencing higher oscillatory shear. We indeed observe low TAWSS and high OSI, RRT and ECAP throughout the thoracic FL. Circumferentially-averaged OSI, ECAP and RRT reach their highest levels at the location of greatest FL growth, surrounding section β. At this location, FL velocity is also most highly decorrelated between IVPs and the highest-energy spatial mode exhibits more noticeable differences than on other planes. Disturbed shear indices are therefore considerably more sensitive to IVP than TAWSS.

Being more reliably measured by 4DMR than WSS indices, flow helicity has recently been associated with FL growth in TBAD patients[34] and has been identified as a surrogate marker of oscillatory shear in carotid arteries[13]. It has also shown high sensitivity to inlet conditions in healthy aortae[28], but this effect has not been previously examined in TBAD. In the ascending aorta, we saw that helicity magnitude is reduced and stronger negative helicity develops when in-plane velocity components are neglected. In the dissected descending aorta, helicity is minimally affected by IVP in the TL but is highly sensitive to it throughout the FL; the temporal development, strength and directionality of helical structures were affected both by in-plane inlet velocity components and inlet flow volume. Time-averaged helicity and helicity magnitude reach near-zero at β, where disturbed shear and aortic growth was highest. Furthermore, in the +25% case, increased helical strength corresponded with a reduction in disturbed shear indices throughout the FL. Together, our results support previous reports[13] that helicity acts to stabilise flow and may be used as a proxy for OSI in the FL when 4DMR data alone are available.

In contrast to section β, TMP, TAWSS and helicity were elevated at α, where considerable growth was also observed. In this region, flow jets through the PET and impinges on the wall. While differences in TAWSS and helicity were observed in the region surrounding section α, as reported in previous studies[1,24], these conditions were not as sensitive to IVP. The contrasting haemodynamic conditions in each of these growth-prone regions suggest that FL growth may be driven by a range of different conditions.

With analysis via POD, the +25% IVP exhibited the greatest differences in normalised modal energy distribution, possessing the least relative energy in mode 1 and a relatively greater amount of energy in higher modes compared with the other flow-matched IVPs. This alteration to modal energy distribution, indicating a higher degree of turbulence and flow complexity, have been observed in other cardiovascular flows when inlet flow rate is increased[19]. Despite these differences in modal energy content, the spatial structure of mode 1 was similar across 3D, TP and +25% cases throughout the descending aorta, echoing the similarities in the development of helicity between these IVPs despite differences in helicity magnitude. The flat IVP held a greater proportion of its energy in mode 1 compared with the other IVPs. Furthermore, it demonstrated dramatic differences in the structure of modes 1 and 2, particularly in the proximal thoracic FL, reflecting the greater differences in helical dynamics in this region compared with the other cases.

Our work supports the general consensus that 3D IVPs should be used where available, with TP IVPs providing the next best option[1,28]. While a flat IVP captured the magnitude and trend of circumferentially-averaged WSS metrics, local values of OSI, ECAP and RRT in the most aneurysmal region exibited considerable differences compared with the 3D IVP. Upon increasing inlet velocity components by 25% to simulate the reported underestimation of velocity by 4DMR[11], the average magnitude of differences in WSS and helicity metrics were greater than any of the flow-matched IVPs. However, our helicity and POD analysis suggest that the +25% IVP better captured the overall flow structure than the flat IVP. Furthermore, our flow decomposition highlights the impact of boundary conditions in the context of reduced order models and ROM-based flow reconstruction.

We conclude that accuracy inlet flow volume *and* velocity distribution are important considerations in capturing oscillatory shear and helicity in the FL, both of which hold predictive potential. As research progresses toward robust, proven links between haemodynamics and disease progression, the use of patient-specific inlet velocity profiles should be prioritised. However, we have seen that existing 4DMR acquisition protocols may not measure this inlet velocity profile with sufficient accuracy. Further work may endeavour to incorporate 2D-Flow MRI data to complement 4DMR data, taking advantage of its higher resolution. Alternatively, the 4DMR imaging domain may be restricted to the ascending aorta alone to facilitate higher spatiotemporal resolution and reduce uncertainty in velocity measurements[11].

As this study has examined only a single case of TBAD, further work to assess the impact of IVP across a wider patient cohort with is warranted. POD analysis across a larger simulation study may illuminate novel links between coherent structures, helicity, oscillatory shear and aneurysmal growth. Furthermore, POD and similar ROM techniques may offer opportunities for 4DMR data enhancement and rapid aortic flow reconstruction, facilitating higher-fidelity haemodynamic data within clinically-relevant timescales[30,27].

Our conclusions must be considered alongside several limitations. Firstly, we have used a rigid wall assumption. Introducing aortic compliance may be expected to reduce the area exposed to high oscillatory shear and low TAWSS which are of particular interest in this study[50,4]. However, the chronicity of this case suggests that the aorta and flap are relatively rigid and the large number of luminal communications should eliminate time shifts in TL and FL pressure waves, limiting the impact of this assumption. This assumption also means that movement of the ascending aorta is neglected, requiring a dynamic mapping of 4DMR data to the static aortic inlet which does not precisely preserve the spatial distribution of

4DMR measurements. However, efforts taken to minimise these effects have been described, and CFD velocity distributions using the 3D IVP closely match 4DMR in the ascending aorta. We have neglected minor aortic branches including the intercostal arteries, a widely-used assumption which is likely cause an elevation of TAWSS, particularly in the abdominal region. However, our focus on the thoracic FL and our equivalent flow should limit the impact of this assumption. The artificial viscosity that results from our use of a RANS turbulence model is likely to affect the energy distribution amongst POD modes; using a highly-resolved laminar simulation may illuminate higher energy content in higher modes. However, the computational expense required is beyond our resource capabilities, and due to the uniformly assumptions across all cases in this study, it should not affect our broader conclusions.

Our results demonstrate that both inlet flow volume and velocity distribution affect potentially predictive haemodynamic quantities in growing regions of the FL. Even 3D IVPs, considered the gold-standard inlet condition, may not provide sufficient accuracy due to 4DMR imaging errors; further efforts may be required to mitigate these errors. As CFD offers unique benefits in the endeavour to assist clinicians in understanding and treating TBAD, further work to reduce uncertainty in inlet conditions and explore their impact using POD analysis is warranted.

Conflict of Interest

The authors express no conflicts of interest.

Acknowledgments

With thanks to funding from the Department of Mechanical Engineering at University College London, the Wellcome-EPSRC Centre for Interventional Surgical Sciences (WEISS) (203145Z/16/Z), the British Heart Foundation (NH/20/1/34705), the Biotechnology and Biological Sciences Research Council (BBSRC) and UK Research and Innovation (UKRI) (BB/X005062/1), and PIONEER (EPSRC-funded, EP/W00481X/1). We also acknowledge support from the Computer Science Department at University College London and use of their high performance computing facilities. We finally thank Nina Montana-Brown and Yipeng Hu for their assistance with image registration.

References

1. C. H. Armour, B. Guo, S. Pirola, S. Saitta, Y. Liu, Z. Dong, X. Y. Xu. The influence of inlet velocity profile on predicted flow in type B aortic dissection. Biomech. Model. Mechanobiol. 20:481–490, 2021.

2. A. Arzani, S. T. M. Dawson. Data-driven cardiovascular flow modeling: examples and opportunities , 2020.

3. A. Bakhshinejad. Novel Algorithms for Merging Computational Fluid Dynamics and 4D Flow MRI. Ph.D. thesis.

4. K. Bäumler, V. Vedula, A. M. Sailer, J. Seo, P. Chiu, G. Mistelbauer, F. P. Chan, M. P. Fischbein, A. L. Marsden, D. Fleischmann. Fluid-structure interaction simulations of patient-specific aortic dissection. Biomech. Model. Mechanobiol. , 2020.

5. M. Berezowski, J. Scheumann, F. Beyersdorf, M. Jasinski, T. Plonek, M. Siepe, M. Czerny, B. Rylski. Early aortic growth in acute descending aortic dissection. Interact. Cardiovasc. Thorac. Surg. 34:857–864, 2022.

6. M. Bonfanti, S. Balabani, J. P. Greenwood, S. Puppala, S. Homer-Vanniasinkam, V. Díaz-Zuccarini. Computational tools for clinical support: a multi-scale compliant model for haemodynamic simulations in an aortic dissection based on multi-modal imaging data. J. R. Soc. Interface 14:20170632, 2017.

7. N. S. Burris, D. A. Nordsletten, J. A. Sotelo, R. Grogan-Kaylor, I. B. Houben, C. A. Figueroa, S. Uribe, H. J. Patel. False lumen ejection fraction predicts growth in type B aortic dissection: preliminary results. Eur. J. Cardiothorac. Surg. 57:896–903, 2020.

8. G. Byrne, F. Mut, J. Cebral. Quantifying the large-scale hemodynamics of intracranial aneurysms. AJNR Am. J. Neuroradiol. 35:333–338, 2014.

9. N. Cagney, S. Balabani. Influence of shear-thinning rheology on the mixing dynamics in Taylor-Couette flow. Chemical Engineering and Technology 42:1680–1690, 2019.

10. F. M. Callaghan, P. Bannon, E. Barin, D. Celemajer, R. Jeremy, G. Figtree, S. M. Grieve. Age-related changes of shape and flow dynamics in healthy adult aortas: A 4D flow MRI study. J. Magn. Reson. Imaging 49:90–100, 2019.

11. M. Cherry, Z. Khatir, A. Khan, M. Bissell. The impact of 4d-flow MRI spatial resolution on patient-specific CFD simulations of the thoracic aorta, 2022.

12. B. Chung, J. R. Cebral. CFD for evaluation and treatment planning of aneurysms: review of proposed clinical uses and their challenges. Ann. Biomed. Eng. 43:122–138, 2015.

13. D. Gallo, D. A. Steinman, P. B. Bijari, U. Morbiducci. Helical flow in carotid bifurcation as surrogate marker of exposure to disturbed shear. J. Biomech. 45:2398–2404, 2012.

14. R. Gottardi, A. Voetsch. Re: False lumen ejection fraction predicts growth in type B aortic dissection: preliminary results. Eur. J. Cardiothorac. Surg. , 2020.

15. L. Grinberg, A. Yakhot, G. E. Karniadakis. Analyzing transient turbulence in a stenosed carotid artery by proper orthogonal decomposition. Ann. Biomed. Eng. 37:2200–2217, 2009.

16. K. Higashigaito, A. M. Sailer, S. M. J. van Kuijk, M. J. Willemink, L. D. Hahn, T. J. Hastie, D. C. Miller, M. P. Fischbein, D. Fleischmann. Aortic growth and development of partial false lumen thrombosis are associated with late adverse events in type B aortic dissection. J. Thorac. Cardiovasc. Surg. 161:1184–1190.e2, 2021.

17. G. Janiga. Quantitative assessment of 4D hemodynamics in cerebral aneurysms using proper orthogonal decomposition. J. Biomech. 82:80–86, 2019.

18. C. Karmonik, M. Müller-Eschner, S. Partovi, P. Geisbüsch, M.-K. Ganten, J. Bismuth, M. G. Davies, D. Böckler, M. Loebe, A. B. Lumsden, H. von Tengg-Kobligk. Computational fluid dynamics investigation of chronic aortic dissection hemodynamics versus normal aorta. Vasc. Endovascular Surg. 47:625–631, 2013.

19. S. Kefayati, T. L. Poepping. Transitional flow analysis in the carotid artery bifurcation by proper orthogonal decomposition and particle image velocimetry. Med. Eng. Phys. 35:898–909, 2013.

20. L. J. Kelsey, J. T. Powell, P. E. Norman, K. Miller, B. J. Doyle. A comparison of hemodynamic metrics and intraluminal thrombus burden in a common iliac artery aneurysm. Int. j. numer. method. biomed. eng. 33, 2017.

21. T. Korpela, S. P. Kauhanen, E. Kariniemi, P. Saari, T. Liimatainen, P. Jaakkola, R. Vanninen, M. Hedman. Flow displacement and decreased wall shear stress might be associated with the growth rate of an ascending aortic dilatation. Eur. J. Cardiothorac. Surg. , 2021.

22. C. A. Kousera, N. B. Wood, W. A. Seed, R. Torii, D. O'Regan, X. Y. Xu. A numerical study of aortic flow stability and comparison with in vivo flow measurements. J. Biomech. Eng. 135:011003, 2013.

23. J. R. Kroeger, F. C. Pavesio, R. Mörsdorf, K. Weiss, A. C. Bunck, B. Baeßler, D. Maintz, D. Giese. Velocity quantification in 44 healthy volunteers using accelerated multi-VENC 4D flow CMR. European Journal of Radiology 137:109570, 2021.

24. Z. Li, S. Liang, H. Xu, M. Zhu, Y. Mei, J. Xiong, D. Chen. Flow analysis of aortic dissection: comparison of inflow boundary conditions for computational models based on 4D PCMRI and doppler ultrasound. Comput. Methods Biomech. Biomed. Engin. pp. 1–12, 2021.

25. S. Madhavan, E. M. C. Kemmerling. The effect of inlet and outlet boundary conditions in image-based CFD modeling of aortic flow. Biomed. Eng. Online 17:66, 2018.

26. D. Marlevi, J. A. Sotelo, R. Grogan-Kaylor, Y. Ahmed, S. Uribe, H. J. Patel, E. R. Edelman, D. A. Nordsletten, N. S. Burris. False lumen pressure estimation in type B aortic dissection using 4D flow cardiovascular magnetic resonance: comparisons with aortic growth. J. Cardiovasc. Magn. Reson. 23:51, 2021.

27. R. McGregor, D. Szczerba, M. von Siebenthal, K. Muralidhar, G. Székely. Exploring the use of proper orthogonal decomposition for enhancing blood flow images via computational fluid dynamics. In: Medical Image Computing and Computer-Assisted Intervention – MICCAI 2008, pp. 782–789, Springer Berlin Heidelberg2008.

28. U. Morbiducci, R. Ponzini, D. Gallo, C. Bignardi, G. Rizzo. Inflow boundary conditions for image-based computational hemodynamics: Impact of idealized versus measured velocity profiles in the human aorta. J. Biomech. 46:102–109, 2013.

29. S. Norouzi, A. Le Floc'h, G. Di Labbio, L. Kadem. Flow examination in abdominal aortic aneurysms: Reduced-order models driven by in vitro data and spectral proper orthogonal decomposition. Phys. Fluids 33:111708, 2021.

30. E. Pajaziti, J. Montalt-Tordera, C. Capelli, R. Sivera, E. Sauvage, S. Schievano, V. Muthurangu. Deep neural networks for fast acquisition of aortic 3D pressure and velocity flow fields. arXiv , 2022.

31. J. Peacock, T. Jones, C. Tock, R. Lutz. The onset of turbulence in physiological pulsatile flow in a straight tube. Experiments in Fluids 24:1–9, 1998.

32. S. Pirola, O. A. Jarral, D. P. O'Regan, G. Asimakopoulos, J. R. Anderson, J. R. Pepper, T. Athanasiou, X. Y. Xu. Computational study of aortic hemodynamics for patients with an abnormal aortic valve: The importance of secondary flow at the ascending aorta inlet. APL Bioeng 2:026101, 2018.

33. A. Rinaudo, G. D'Ancona, J. J. Lee, G. Pilato, A. Amaducci, R. Baglini, F. Follis, M. Pilato, S. Pasta. Predicting outcome of aortic dissection with patent false lumen by computational flow analysis. Cardiovasc. Eng. Technol. 5:176–188, 2014.

34. A. Ruiz-Muñoz, A. Guala, L. Dux-Santoy, G. Teixidó-Turà, M. L. Servato, F. Valente, J. Garrido-Oliver, L. Galian-Gay, L. Gutiérrez, R. Fernandez-Galera, G. Casas, T. González-Alujas, H. Cuéllar-Calabria, K. M. Johnson, O. Wieben, I. Ferreira-Gonzalez, A. Evangelista, J. Rodriguez-Palomares. False lumen rotational flow and aortic stiffness are associated with aortic growth rate in patients with chronic aortic dissection of the descending aorta: a 4D flow cardiovascular magnetic resonance study. J. Cardiovasc. Magn. Reson. 24:20, 2022.

35. E. K. Shang, D. P. Nathan, R. M. Fairman, J. E. Bavaria, R. C. Gorman, J. H. Gorman, B. M. Jackson. Use of computational fluid dynamics studies in predicting aneurysmal degeneration of acute type B aortic dissections — elsevier enhanced reader. https://www.sciencedirect.com/science/article/pii/S0741521415003006/pdfft?isDTMRedir=true&download=true.

36. F. Squizzato, M. C. Hyun, I. Sen, M. D. Oria, T. Bower, G. Oderich, J. Colglazier, R. R. De Martino. Predictors of Long-Term aortic growth and disease progression in patients with aortic dissection, intramural hematoma, and penetrating aortic ulcer. Ann. Vasc. Surg. , 2021.

37. C. Stokes, M. Bonfanti, Z. Li, J. Xiong, D. Chen, S. Balabani, V. Díaz-Zuccarini. A novel MRI-based data fusion methodology for efficient, personalised, compliant simulations of aortic haemodynamics, 2021.

38. E. Sueyoshi, I. Sakamoto, K. Hayashi, T. Yamaguchi, T. Imada. Growth rate of aortic diameter in patients with type B aortic dissection during the chronic phase. Circulation 110:II256–61, 2004.

39. G. Tomaiuolo, A. Carciati, S. Caserta, S. Guido. Blood linear viscoelasticity by small amplitude oscillatory flow. Rheol. Acta 55:485–495, 2016.

40. G. H. W. van Bogerijen, J. L. Tolenaar, V. Rampoldi, F. L. Moll, J. A. van Herwaarden, F. H. W. Jonker, K. A. Eagle, S. Trimarchi. Predictors of aortic growth in uncomplicated type B aortic dissection. J. Vasc. Surg. 59:1134–1143, 2014.

41. H. Wang, D. Balzani, V. Vedula, K. Uhlmann, F. Varnik. On the potential Self-Amplification of aneurysms due to tissue degradation and blood flow revealed from FSI simulations. Front. Physiol. 12:785780, 2021.

42. N. Westerhof, N. Stergiopoulos, M. Noble. Snapshots of Hemodynamics: An Aid for Clinical Research and Graduate Education, New York, New York. pp. 191,246: Springer US2010, 2 edition.

43. H. Xu, D. Baroli, A. Veneziani. Global sensitivity analysis for Patient-Specific aortic simulations: the role of geometry, boundary condition and LES modeling parameters. J. Biomech. Eng. , 2020.

44. H. Xu, Z. Li, H. Dong, Y. Zhang, J. Wei, P. N. Watton, W. Guo, D. Chen, J. Xiong. Hemodynamic parameters that may predict false-lumen growth in type-b aortic dissection after endovascular repair: A preliminary study on long-term multiple follow-ups. Med. Eng. Phys. 50:12–21, 2017.

45. H. Xu, M. Piccinelli, B. G. Leshnower, A. Lefieux, W. R. Taylor, A. Veneziani. Coupled Morphological–Hemodynamic computational analysis of type B aortic dissection: A longitudinal study. Ann. Biomed. Eng. 46:927–939, 2018.

46. P. Youssefi, A. Gomez, C. Arthurs, R. Sharma, M. Jahangiri, C. Alberto Figueroa. Impact of Patient-Specific inflow velocity profile on hemodynamics of the thoracic aorta. J. Biomech. Eng. 140, 2018.

47. P. Yu, V. Durgesh. Comparison of flow behavior in saccular aneurysm models using proper orthogonal decomposition .

48. P. Yu, V. Durgesh, T. Xing, R. Budwig. Application of proper orthogonal decomposition to study coherent flow structures in a saccular aneurysm. J. Biomech. Eng. 143, 2021.

49. J. Zhang, S. M. Rothenberger, M. C. Brindise, M. Markl, V. L. Rayz, P. P. Vlachos. Wall shear stress estimation for 4D flow MRI using Navier-Stokes equation correction. Ann. Biomed. Eng. , 2022.

50. T. Zhu, O. Mian, M. Boodhwani, L. Beauchesne, C. Dennie, K. Chan, G. A. Wells, F. Rubens, T. Coutinho. Combining aortic size with arterial hemodynamics enhances assessment of future thoracic aortic aneurysm expansion. Can. J. Cardiol. , 2022.

51. Y. Zhu, S. Mirsadraee, G. Asimakopoulos, A. Gambaro, U. Rosendahl, J. Pepper, X. Y. Xu. Association of hemodynamic factors and progressive aortic dilatation following type a aortic dissection surgical repair. Sci. Rep. 11:11521, 2021.